ACS Catalysis

pubs.acs.org/acscatalysis

Research Article

Solar-Enhanced Plasma-Catalytic Oxidation of Toluene over a Bifunctional Graphene Fin Foam Decorated with Nanofin-like MnO_2

Zheng Bo, Shiling Yang, Jing Kong, Jinhui Zhu, Yaolin Wang, Huachao Yang,* Xiaodong Li, Jianhua Yan,* Kefa Cen, and Xin Tu*

Cite This: *ACS Catal.* 2020, 10, 4420−4432

Read Online

ACCESS | Metrics & More | Article Recommendations | Supporting Information

ABSTRACT: In this work, we propose a hybrid and unique process combining solar irradiation and post-plasma catalysis (PPC) for the effective oxidation of toluene over a highly active and stable MnO_2/GFF (bifunctional graphene fin foam) catalyst. The bifunctional GFF, serving as both the catalyst support and light absorber, is decorated with MnO_2 nanofins, forming a hierarchical fin-on-fin structure. The results show that the MnO_2/GFF catalyst can effectively capture and convert renewable solar energy into heat (absorption of >95%), leading to a temperature rise (55.6 °C) of the catalyst bed under solar irradiation (1 sun, light intensity 1000 W m^{-2}). The catalyst weight (9.8 mg) used in this work was significantly lower (10−100 times lower) than that used in previous studies (usually 100−1000 mg). Introducing solar energy into the typical PPC process via solar thermal conversion significantly enhances the conversion of toluene and CO_2 selectivity by 36−63%, reaching ∼93% for toluene conversion and ∼83% for CO_2 selectivity at a specific input energy of ∼350 J L^{-1}, thus remarkably reducing the energy consumption of the plasma-catalytic gas cleaning process. The energy efficiency for toluene conversion in the solar-enhanced post-plasma catalytic (SEPPC) process reaches up to 12.7 g kWh^{-1}, ∼57% higher than that using the PPC process without solar irradiation (8.1 g kWh^{-1}), whereas the energy consumption of the SEPPC process is reduced by 35−52%. Moreover, the MnO_2/GFF catalyst exhibits an excellent self-cleaning capability induced by solar irradiation, demonstrating a superior long-term catalytic stability of 72 h at 1 sun, significantly better than that reported in previous works. The prominent synergistic effect of solar irradiation and PPC with a synergistic capacity of ∼42% can be mainly attributed to the solar-induced thermal effect on the catalyst bed, boosting ozone decomposition (an almost triple enhancement from ∼0.18 g_{O_3} g^{-1} h^{-1} for PPC to ∼0.52 g_{O_3} g^{-1} h^{-1} for SEPPC) to generate more oxidative species (e.g., O radicals) and enhancing the catalytic oxidation on the catalyst surfaces, as well as the self-cleaning capacity of the catalyst at elevated temperatures driven by solar irradiation. This work opens a rational route to use abundant, renewable solar power to achieve high-performance and energy-efficient removal of volatile organic compounds.

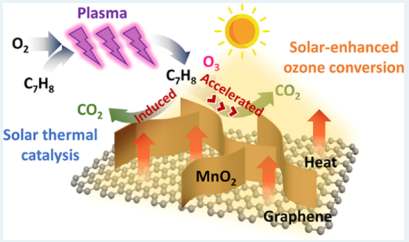

KEYWORDS: *volatile organic compounds, plasma-catalysis, toluene oxidation, solar thermal conversion, hierarchical fin-on-fin structure*

1. INTRODUCTION

Air pollution remains a global environmental problem and has significant harmful effects on human health and the environment. Exposure to air pollution is estimated to have contributed to more than four million deaths in 2015 because of increased mortality and morbidity from cardiovascular and respiratory disease, as well as lung cancer.[1] Volatile organic compounds (VOCs) are an important source of air pollutants and play a significant role in the formation of photochemical smog and haze.[2−6] Plasma-catalysis, the combination of nonthermal plasma (NTP) and heterogeneous catalysis, has been demonstrated as a promising technology for the effective removal of VOCs in low concentrations at low temperatures.[7,8] In a plasma-catalysis system, catalysts can be packed inside the plasma zone (in-plasma catalysis, IPC) or placed downstream of the plasma zone (post-plasma catalysis, PPC).[9−11] The coupling of NTP with suitable catalysts can generate a plasma-catalysis synergy,[12−14] enhancing the conversion of VOCs, the selectivity to CO_2, and the energy efficiency of the hybrid process, while reducing the formation of undesirable by-products.[15,16] However, catalyst stability remains a key barrier in the development of a plasma-catalytic gas cleaning process for the removal of VOCs, especially when using IPC because of complex physicochemical interactions between plasma and the catalyst and limited available knowledge of designing highly active and stable catalysts effective in the IPC processes.[3,9] In contrast, PPC integrates the two relatively independent processes of NTP and well-developed catalytic oxidation, where plasma-generated ozone can be effectively converted to more active oxygen atoms on catalyst surfaces to achieve

Received: November 8, 2019
Revised: February 27, 2020
Published: March 25, 2020

https://dx.doi.org/10.1021/acscatal.9b04844
ACS Catal. 2020, 10, 4420−4432

superior conversion of VOCs and CO_2 selectivity, showing great potential to be used on a commercial scale.[17,18] However, further increasing the energy efficiency for VOC conversion is of primary importance to make the plasma-catalytic gas cleaning technology more attractive and economically competitive.

The overall energy efficiency of a PPC process can be manipulated by tuning either the plasma process, the catalytic process, or both.[17] Increasing the plasma energy input in a PPC process can enhance the conversion of VOCs while keeping the initial concentration of VOCs constant.[19−21] However, this usually results in a decreased energy efficiency of PPC processes. Catalysts have been demonstrated to play an important role in PPC processes. Thus, designing innovative, highly active, and stable catalytic materials as well as alternative efficient catalytic routes is critical to tackling these challenges. Nanomaterials have shown significant potential in heterogeneous catalysis for environmental and energy applications with superior catalytic performance compared to bulk catalysts because of their unique physical and chemical properties. However, limited efforts have been dedicated to the integration of NTP with catalytic nanomaterials for the removal of VOCs in plasma-catalytic processes. In addition to the judicious design of high-performance catalysts,[22−24] using external heating to elevate the temperature of the catalyst bed in PPC processes has been commonly used as an effective way to enhance catalyst activities for the oxidation of VOCs.[22,25−27] Increasing the temperature of the catalyst bed can facilitate the activation of lattice oxygen and promote ozone conversion on the catalyst surfaces, thus significantly enhancing catalytic oxidation of VOCs.[28−30] Rezaei et al. investigated the oxidation of toluene by ozone with a temperature-controlled MnO_x/γ-Al_2O_3 catalyst bed.[31−33] They found that efficient toluene conversion (>90%) and ozone conversion (∼100%) can be achieved by raising the temperature of the catalyst bed from room temperature to 80−100 °C. Compared to the catalyst bed without heating, heating the catalyst bed to >65 °C enhances the stability of the catalyst. However, using external heating to elevate the temperature of the catalyst bed to achieve the enhanced oxidation of VOCs consumes additional energy. Therefore, achieving high-performance removal of VOCs and ultra-low energy consumption simultaneously in PPC processes remains a significant challenge.

Solar energy, the largest renewable energy source, has attracted significant interest in emerging fields such as chemical synthesis, water splitting, CO_2 conversion, solar thermal conversion, and so on.[34,35] It is, therefore, a rational strategy to exploit and use low-cost renewable solar energy to drive catalytic reactions. Solar thermal conversion is a promising approach to use solar energy, where the incident light is harvested by light absorbers and effectively converted into heat.[36] Therefore, combining renewable and sustainable solar power with a PPC process via solar thermal conversion has significant potential to open a new route for the solar-driven effective catalytic conversion of VOCs with low energy costs.

The rational design of the catalysts is crucial for efficiently utilizing solar irradiation to drive catalytic reactions. Graphene has been widely used as a catalyst support.[37−39] Graphene fin foam (GFF) with a three-dimensional (3D) interconnected architecture has been investigated for a range of energy applications including energy storage and solar-steam generation.[40,41] The unique advantages of graphene, including inherent broad spectral absorption, high thermal conductivity, and excellent solar thermal conversion capacity, make this material an ideal light absorber.[42] In addition, GFF has a non-agglomerated interconnected morphology, an enlarged accessible surface area, and sharp exposed edges, all of which are favorable in enhancing catalyst dispersion and catalytic activity.[43] MnO_2 has been demonstrated as an efficient catalyst in PPC processes as it can effectively convert ozone into active oxygen species.[44] Therefore, the integration of GFF and MnO_2 has excellent potential to achieve remarkable solar thermal conversions and efficient plasma catalytic reactions.

In this work, we propose for the first time a novel solar-enhanced post-plasma catalytic (SEPPC) process for the oxidation of toluene, a model VOC, over a nanofin-like MnO_2 catalyst decorated on a bifunctional GFF in a coaxial dielectric barrier discharge (DBD) plasma reactor. GFF, as both a catalyst support and a light absorber, was synthesized using plasma-enhanced chemical vapor deposition (PECVD). Nanofin-like MnO_2 was then decorated on GFF as a high-performance catalyst via a facile redox reaction, generating a hierarchical fin-on-fin structure. To the best of our knowledge, such a novel catalytic nanomaterial with a hierarchical fin-on-fin structure has not been investigated in plasma-catalytic processes before. The influence of the catalyst and solar illumination (1 sun) on the oxidation of toluene has been investigated in terms of the conversion of toluene, CO_2 selectivity, ozone conversion, and energy efficiency. Moreover, excellent catalyst stability toward toluene conversion and CO_2 selectivity has been demonstrated. The contributions of the PPC, solar thermal catalysis (STC), and their synergistic effect to the SEPPC oxidation of toluene have been discussed.

2. EXPERIMENTAL SECTION

2.1. Synthesis of GFF. GFF was prepared using the PECVD method in a temperature-controlled radio-frequency inductively coupled plasma (ICP) system. Nickel powders with an average particle size of 5 μm were spread on a quartz slide (120 mm × 40 mm) and placed in the plasma chamber (quartz tube). The chamber was pumped to a low pressure of 3 Pa before the synthesis. When the plasma system was switched off, the sample (Ni powders) was heated to 900 °C and cooled down to 700 °C. The ICP system was then switched on, generating plasma in the quartz tube using mixed hydrogen (5 mL min^{-1}) and methane (5 mL min^{-1}) at a constant pressure of 28 Pa and a fixed power of 250 W for the growth of graphene fins (GF). After the synthesis, the plasma chamber was cooled to room temperature under vacuum conditions. The obtained GF/Ni foam was functionalized by 240 ppm moist ozone (humidified by passing through a water bubble bottle) in air (250 mL min^{-1}) for 5 min. After dissolving Ni scaffolds with a 3 M HCl solution at 80 °C for 12 h, the samples were freeze-dried for 8 h.

2.2. MnO_2 Deposition on GFF. MnO_2 was loaded on GFF by the facile redox reaction between graphene and $KMnO_4$. GFF was immersed into a $KMnO_4$ solution (1067 mg of $KMnO_4$ dissolved in 160 mL of deionized water) at 80 °C for 18 h in an oven. Afterward, the residual $KMnO_4$ was removed by washing the sample several times using deionized water. The freeze-dried sample was annealed at 400 °C for 4 h under vacuum conditions to obtain MnO_2/GFF.

2.3. Synthesis of MnO_2. Pure MnO_2 was synthesized via the reduction of $KMnO_4$ using a similar method for the synthesis of MnO_2/GFF. Sulfuric acid (2 mL, 98 wt %) was

https://dx.doi.org/10.1021/acscatal.9b04844
ACS Catal. 2020, 10, 4420−4432

slowly dropped into a $KMnO_4$ solution (1067 mg of $KMnO_4$ dissolved in 160 mL of deionized water). Cu foil (8 × 8 cm^2) was then immersed in the $KMnO_4$ solution and heated at 80 °C for 18 h in an oven. After that, the precipitate was filtered, washed using deionized water, and dried at 80 °C to obtain pure MnO_2.

2.4. Characterization. The morphologies of GFF and MnO_2/GFF were analyzed using a SU-70 scanning electron microscope (SEM, Hitachi). The elemental distribution (Mn, O, and C) was investigated by the energy-dispersive spectroscopy (EDS, Oxford Instruments) technique. The dispersion of MnO_2 on GFF and the corresponding elemental mapping were determined by using transmission electron microscopy (TEM, JEM-2100; JEOL, Japan) equipped with an Oxford Instruments X-MAX EDS system. The crystal structures of GFF and MnO_2/GFF were characterized by X-ray diffraction (XRD) using a PANalytical X'Pert diffractometer equipped with Ni β-filtered Cu Kα radiation. The surface chemical states of GFF and MnO_2/GFF were measured by X-ray photoelectron spectroscopy (XPS, VG Escalab Mark II) with a monochromatic Mg Kα X-ray source ($h\nu$ = 1253.6 eV, West Sussex). The binding energies of the spectra were calibrated with the C 1s photoemission peak at 284.6 eV. Raman spectra of both samples were recorded using a LabRAM HR Evolution Raman spectrometer (Horiba Jobin Yvon). Infrared spectra of GFF and MnO_2/GFF were measured using a Fourier transform infrared (FTIR) spectrometer (Thermo Fisher, Nicolet 5700). Diffuse reflectance UV−vis−infrared absorption of the samples was performed on a spectrophotometer (Shimadzu UV-3150). An infrared (IR) thermographic camera (FLIR ThermaCAM S65, USA) was used to record the IR images of GFF and MnO_2/GFF under simulated solar irradiation. The window of the catalytic reactor was removed for the IR measurements. The weight loading of Mn in MnO_2/GFF was 17.4 wt %, measured by inductively coupled plasma−mass spectrometry (XSENIES, Thermo Electron Corporation). The hydrogen temperature-programmed reduction (H_2-TPR) analysis of the catalyst was carried out using a chemisorption analyzer (Micrometrics, Autochem II 2920). The Brunauer−Emmett−Teller (BET) surface area of the samples was determined via N_2 adsorption−desorption measurements at −196 °C (Micromeritics TriStar II). Diffuse reflectance infrared Fourier transform spectroscopy (DRIFTS) analysis of the fresh (before reaction) and spent catalysts after the SEPPC and PPC reactions was carried out on an FTIR spectrometer (Thermo Fisher, Nicolet 460) equipped with a deuterated triglycine sulfate detector. The organic intermediates deposited on the catalyst surfaces (PPC reaction for 8 h) were extracted using a methanol solution under ultrasonic vibration for 1 h and then analyzed by gas chromatography−mass spectrometry (GC−MS, QP2010SE, Shimadzu).

2.5. Experimental Setup. Figure 1 shows the schematic diagram of the SEPPC system for gas clean-up, consisting of a typical post-plasma catalytic reactor coupled with a solar irradiation unit for the catalyst bed. A 2 mm-long stainless-steel mesh was wrapped around a quartz tube (external diameter 7 mm and inner diameter 5 mm) and used as a ground electrode, whereas a stainless-steel rod with a diameter of 4 mm was placed in the quartz tube, acting as the high-voltage electrode. The DBD reactor was connected to a high voltage alternating-current (ac) power supply (CTP-2000K, Suman Plasma Technology). Air (zero grade, Gingergas) was used as the carrier gas with a fixed flow rate of 250 mL min^{-1}. A high-

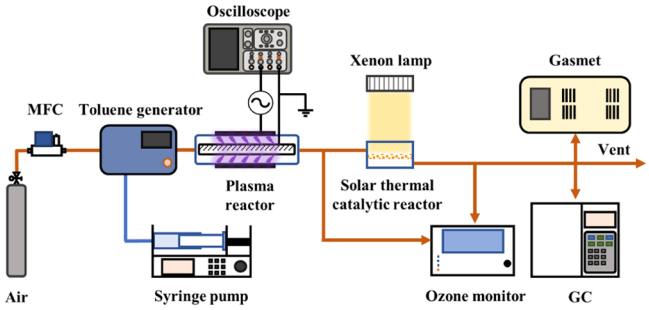

Figure 1. Schematic diagram of the SEPPC system.

resolution syringe pump (LSP01-1BH, Longer Precision Pump) was used to inject liquid toluene into a toluene generator (FD-PG, Friend Laboratory Equipment) to form a toluene vapor of 260 ppm in air. The electrical signals of the DBD were monitored using a digital oscilloscope (MDO 3034, Tektronix). A solar-driven catalytic reactor with a quartz window was placed downstream of the DBD reactor. To reduce heat loss during the solar irradiation, a piece of the MnO_2/GFF catalyst (diameter of 35 mm and weight of 9.8 mg) was covered on thermal insulation and was placed on a porous tray in the solar-driven catalytic reactor. For comparison, the catalytic activities of pure MnO_2 (powder, 9.8 mg) and GFF (35 mm in diameter) were also investigated. Instead of using conventional heating for the catalyst bed, renewable solar power was used to thermally activate the catalyst bed in this work. A xenon lamp (Microsolar300A, Perfectlight Technology) was placed over the catalytic reactor and used as a light source to produce an AM1.5G (air mass 1.5, global) spectrum between 320 and 2500 nm. The light intensity was maintained at 1000 W m^{-2} (corresponding to 1 sun) by controlling the light current (12 A) and the distance between the xenon lamp and the catalyst bed (37.3 cm). The oxidation of toluene was investigated under different process modes: NTP-only, PPC (without solar irradiation), SEPPC, and catalytic oxidation with and without solar irradiation. The plasma oxidation of toluene (NTP-only) was carried out at room temperature and atmospheric pressure in the DBD reactor, whereas no external heating was used in the PPC without the use of solar irradiation. The solar-enhanced PPC experiment was tested under the solar irradiation (1 sun). In addition, a catalyst stability test of 72 h for the PPC and SEPPC processes was carried out at a constant specific input energy (SIE) of 364 J L^{-1}. Catalytic oxidation of toluene in air, in both the dark and under sun radiation (1 sun) was also carried out with plasma off to better understand the role of ozone and the solar-induced temperature effect on this reaction. The operating conditions (catalyst amount, toluene concentration, and total gas flow) used in this reaction were kept the same as those used in NTP-only, PPC, and SEPPC processes. In addition, no ozone was involved in the catalytic oxidation of toluene.

The concentrations of toluene and CO_2 were measured using gas chromatography (GC9790Plus, Fuli Instruments) equipped with two flame ionization detectors and a reformer furnace. Ozone was analyzed with an ozone monitor (Models 106-MH, 2B Technology) before and after the solar thermal catalytic reactor to understand the contributions of the catalyst to the conversion of ozone. The formation of byproducts was monitored using a portable FTIR gas analyzer (Gasmet Dx4000, Finland). The outlet gas was fed into the Gasmet

https://dx.doi.org/10.1021/acscatal.9b04844
ACS Catal. 2020, 10, 4420−4432

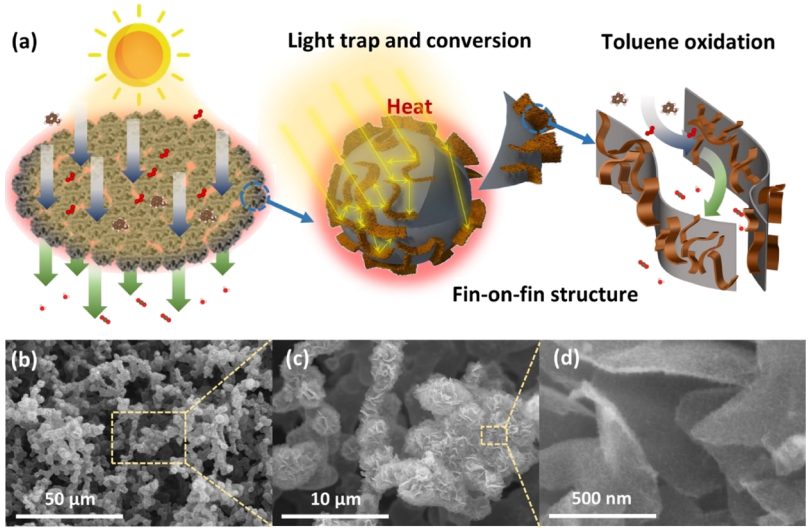

Figure 2. (a) Schematic illustration of a hierarchical fin-on-fin catalyst for light harvest and toluene oxidation. (b–d) SEM images of the MnO_2/GFF catalyst.

gas cell. The FTIR spectra of the gas phase byproducts were recorded in the wavenumber range of 600–4250 cm^{-1}.

The regeneration of deactivated catalysts with ozone under solar irradiation was investigated. In this test, a fresh MnO_2/GFF catalyst was used for toluene oxidation in the PPC process without solar irradiation (dark) for 2 h, followed by an oxidative regeneration with ozone (250 ppm) under solar irradiation (1 sun) for 1 h. The ozone was generated by NTP using the same DBD reactor. The flow rate of air was maintained at 250 mL min^{-1} in the process.

The SIE is defined as the energy dissipated per unit volume of the gas flow as

$$\mathrm{SIE(J\ L^{-1})} = \frac{P}{Q} \times 60 \tag{1}$$

where the discharge power (P) of the DBD reactor is determined using the Lissajous method,[45] and Q is the total gas flow rate.

The ozone conversion (η_{O_3}), toluene conversion ($\eta_{C_7H_8}$), CO_2 selectivity (S_{CO_2}), CO selectivity (S_{CO}), carbon balance, energy efficiency (η_{EY}), ozone decomposition capacity (ODC), and synergistic capacity (SC) of the SEPPC process are defined as

$$\eta_{O_3}(\%) = \frac{[O_3]_0 - [O_3]_{out}}{[O_3]_0} \times 100 \tag{2}$$

$$\eta_{C_7H_8}(\%) = \frac{[C_7H_8]_{in} - [C_7H_8]_{out}}{[C_7H_8]_{in}} \times 100 \tag{3}$$

$$S_{CO_2}(\%) = \frac{[CO_2]_{out}}{7 \times \eta_{C_7H_8} \times [C_7H_8]_{in}} \times 100 \tag{4}$$

$$S_{CO}(\%) = \frac{[CO]_{out}}{7 \times \eta_{C_7H_8} \times [C_7H_8]_{in}} \times 100 \tag{5}$$

$$\text{Carbon balance}\ (\%) = S_{CO_2} + S_{CO} \tag{6}$$

$$\eta_{EY}(\mathrm{g\ kWh^{-1}}) = \frac{3.6 \times M \times \eta_{C_7H_8} \times [C_7H_8]_{in}}{24.04 \times SIE} \tag{7}$$

$$\mathrm{ODC(g_{O_3}\ g^{-1}\ h^{-1})} = \frac{6 \times 10^{-5} \times M_{O_3} \times Q \times \eta_{O_3} \times [O_3]_0}{24.04} \tag{8}$$

$$SC(\%) = \frac{\eta_{SEPPC} - \eta_{PPC} - \eta_{STC}}{\eta_{PPC} + \eta_{STC}} \tag{9}$$

where $[O_3]_0$ is the concentration of ozone measured before the catalyst bed; $[O_3]_{out}$ is the concentration of ozone at the outlet of the catalyst bed; $[C_7H_8]_{in}$ and $[C_7H_8]_{out}$ are the inlet and outlet concentrations of toluene, respectively; $[CO_2]_{out}$ and $[CO]_{out}$ are the concentrations of generated CO_2 and CO, respectively; M and M_{O_3} are the molar mass of toluene and ozone, respectively; η_{SEPPC}, η_{PPC}, and η_{STC} are the toluene conversion of SEPPC, PPC, and STC processes, respectively.

3. RESULTS AND DISCUSSION

3.1. Characterization of the MnO_2/GFF Catalyst.

Figure 2a illustrates the hierarchical fin-on-fin structure of the MnO_2/GFF catalyst. Bifunctional GFF, serving as the catalyst support and light absorber, can efficiently trap the incident light and convert the absorbed solar energy to heat, thus elevating the temperature of the catalytic reaction. Meanwhile, the nanofin-like MnO_2 catalyst can effectively turn ozone into active oxygen species, thus enhancing the oxidation of toluene on the catalytic surface.

Figure 2b–d shows the surface morphologies of GFF and MnO_2/GFF. GFF presents a 3D interconnected macroporous structure, which is beneficial for gas transport in the oxidation of toluene (Figure 2b). A close-up view in Figure 2c indicates that GFF is composed of dense fins with exposed sharp edges, in a vertical orientation, and with a non-agglomerated morphology. Because of the multiple reflections in the dense fins, GFF can trap and almost fully absorb the incident light, effectively converting the absorbed solar energy into heat.[40,41] In addition, GFF provides an abundance of sites for uniform dispersion of the nanofin-like MnO_2 on its surface, forming a hierarchical fin-on-fin structure (Figure 2d). The open channels and non-agglomerated morphology of MnO_2 nanofins facilitate gas diffusion and enlarge the accessible surface

https://dx.doi.org/10.1021/acscatal.9b04844
ACS Catal. 2020, 10, 4420–4432

area in the catalytic reaction.[46] As shown in Figure S1 (Supporting Information), the element mapping of the catalyst indicates the presence of a graphene framework and a homogeneous distribution of MnO_2 on GFF. The photos of the samples in the different steps of the synthesis can be found in Figure S2 (Supporting Information). Compared to the pristine nickel foam, GFF and MnO_2/GFF are black and exhibit an excellent absorption within visible wavelengths. Both samples retain a freestanding and monolithic structure after HCl etching and MnO_2 deposition, which can be ascribed to the formation of a densely interconnected network of GFF. In addition, the size of GFF and MnO_2/GFF can be extended by using a larger nickel foam as a template for harvesting more solar energy in practical applications.

Figure 3a,b presents the surface chemical states of MnO_2, GFF, and MnO_2/GFF. The full-range XPS analysis of GFF

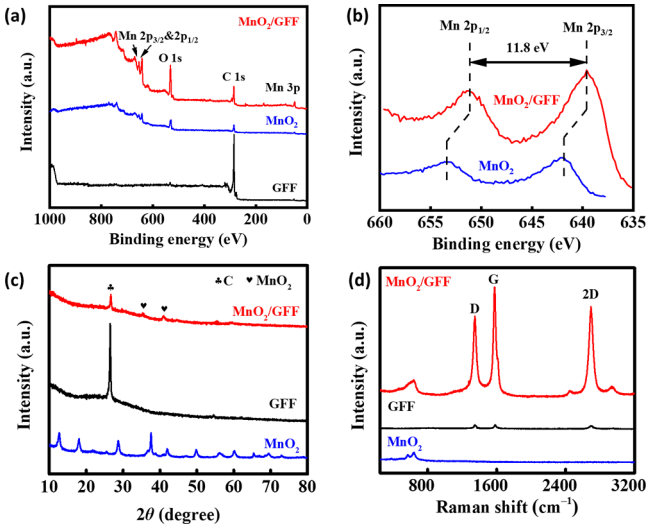

Figure 3. Characterization of MnO_2, GFF, and MnO_2/GFF. (a) XPS survey spectra, (b) Mn 2p spectra, (c) XRD patterns, and (d) Raman spectra.

shows the presence of carbon in GFF, whereas the existence of manganese oxide after the deposition of MnO_2 onto GFF can be observed (Figure 3a). The XPS spectrum of pure MnO_2 is similar to that of MnO_2/GFF. A spin-energy separation of 11.8 eV between Mn $2p_{1/2}$ and Mn $2p_{3/2}$ further confirms the presence of MnO_2 in MnO_2/GFF (Figure 3b).[47] The average oxidation state (AOS) of MnO_2 and MnO_2/GFF was estimated based on the Mn 3s spectra using the equation: $AOS = 8.956 - 1.126 \times \Delta Es$, where ΔEs represents the difference of peak energies between the doublet Mn 3s peaks.[48] The AOS of MnO_2 and MnO_2/GFF was 3.60 and 3.21, respectively (Figure S3, Supporting Information), suggesting that both MnO_2 and MnO_2/GFF have an intermediate oxidation state between Mn^{4+} and Mn^{3+}. The loading of MnO_2 on GFF can reduce the average oxidation state of Mn, which could facilitate the conversion of ozone to enhance the oxidation of toluene in the PPC process.[32] The binding energy of the Mn $2p_{3/2}$ peak in the MnO_2/GFF catalyst shifts to a lower value (639.6 eV) compared to that of the as-prepared MnO_2 (641.8 eV), which can be attributed to the incorporation of MnO_2 into the graphene resulting in an increased chargeability of Mn atoms.[49,50] The downshift phenomenon can be ascribed to an increased π electron cloud density because of the introduction of graphene. The hybridization between graphene and MnO_2 at the interface reduced the electronic localization and extended the π conjugated systems. As a result, the interfacial charge transfer from graphene promoted the chargeability of Mn atoms. The XRD patterns of both samples exhibit a dominant characteristic peak at 26°, which correlates with the (002) diffraction of graphitic carbon in GFF and MnO_2/GFF (Figure 3c),[51,52] whereas the two peaks at 2θ = 36 and 41° in the XRD of MnO_2/GFF are associated with the (400) and (420) lattice planes of standard α-MnO_2 (JCPDS 44-0141), respectively.[53,54] The magnified XRD patterns of the samples at 30−50° are presented in Figure S4 (Supporting Information). Moreover, the broad and weak MnO_2 peaks present in the XRD pattern of MnO_2/GFF suggest the formation of a low crystallinity of MnO_2, resulting in high dispersion of MnO_2 on GFF,[55] which can be further validated by the TEM images of MnO_2/GFF. In addition, the characteristic peaks of MnO_2 can be indexed to standard α-MnO_2 (JCPDS 44-0141), indicating that the as-prepared MnO_2 has high purity and crystallinity. As shown in Figure S5 (Supporting Information), MnO_2 nanoparticles with a diameter of 10−15 nm are uniformly dispersed on the surface of GFF. The lattice spacings of 0.248 and 0.214 nm for MnO_2, correspond to the (400) and (420) lattice planes of standard α-MnO_2 (Figure S5c,d, Supporting Information), respectively, which agrees well with the XRD results. As shown in Figure S6 (Supporting Information), the elemental mapping has demonstrated the presence of well-defined dispersion of Mn and O on the graphene layer, which is consistent with the distribution of nanoparticles. Figure 3d shows the structural and electronic properties of both samples using Raman spectra. The peaks at ~630 cm^{-1} in the spectra of MnO_2 and MnO_2/GFF can be ascribed to Mn−O lattice vibration in the [MnO_6] octahedral.[56,57] The H_2-TPR profile of MnO_2/GFF is given in Figure S7 (Supporting Information). Two peaks of H_2 consumption at 296 and 353 °C are associated with the reduction of MnO_2 to Mn_3O_4 and the reduction of Mn_3O_4 to MnO, respectively.[58] The presence of low reduction temperatures in the TPR profile of MnO_2/GFF indicates the low temperature reducibility of the catalyst and the formation of high-mobility oxygen species on the catalyst surfaces, as confirmed in previous works.[59−61] The BET surface area of GFF and MnO_2/GFF was 29.2 and 26.7 $m^2\ g^{-1}$, respectively.

The light absorption ability of MnO_2, GFF, and MnO_2/GFF was evaluated using UV−vis−infrared analysis. As shown in Figure 4a, the absorption of MnO_2 significantly decreases when the spectrum changes from the UV and visible region to the

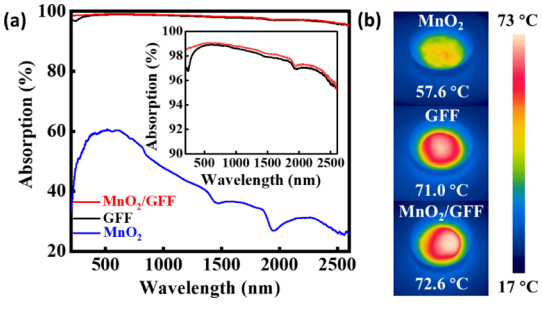

Figure 4. (a) UV−vis−infrared spectra and (b) IR images of MnO_2, GFF, and MnO_2/GFF at 1 sun.

https://dx.doi.org/10.1021/acscatal.9b04844
ACS Catal. 2020, 10, 4420−4432

infrared region, indicating that pure MnO_2 does not have an efficient light absorption capability (≤60%) in the entire solar spectrum. By contrast, both GFF and MnO_2/GFF show an ultrahigh absorption of >95% across the whole solar spectrum, which significantly improves the light utilization efficiency, especially in the infrared region. Figure 4b shows the IR images of MnO_2, GFF, and MnO_2/GFF under solar irradiation (1 sun). The steady-state surface temperatures of MnO_2, GFF, and MnO_2/GFF were 57.6, 71.0, and 72.6 °C, respectively, demonstrating that both GFF and MnO_2/GFF have a high solar-to-thermal conversion efficiency (13.4−15 °C higher than that of MnO_2). Moreover, the time-dependent variation of temperature under solar illumination reveals that MnO_2/GFF exhibits a faster temperature, and an increased response compared with pure MnO_2 (Figure S8, Supporting Information). Thus, GFF not only traps and converts the solar irradiation but also transfers heat from the graphene support to MnO_2 because of its excellent thermal conductivity. The maximum surface temperature change (54.0−55.6 °C at 1 sun) is more significant than that reported in previous works using graphene foam-based nanomaterials (33.5−39 °C at 1 sun).[40,41] The solar-thermal conversion efficiency η_{st} was estimated to be ∼62.2% based on the energy balance between the converted thermal energy $\dot{Q}_{in}$ and the heat dissipation $\dot{Q}_{surr}$ (see the Supporting Information & Figure S8 for details).

3.2. Toluene Oxidation under Different Process Modes. Figure 5 shows the influence of SIE on the oxidation of toluene using different processes (NTP-only, PPC, and SEPPC). Increasing the SIE from 144 to 382 J L^{-1} enhances the conversion of toluene and CO_2 selectivity but decreases the energy efficiency for toluene conversion in all three processes. At a fixed SIE, the performance of the PPC process is better than that using NTP-only, whereas the combination of PPC oxidation with solar irradiation (1 sun) further enhances the conversion of toluene and CO_2 selectivity, as well as the energy efficiency of the hybrid process. For instance, compared to the PPC process, the conversion of toluene and CO_2 selectivity in the SEPPC process were enhanced by 63 and 36%, respectively, reaching up to ∼93 and ∼83% at an SIE of ∼350 J L^{-1}.

Compared to the NTP-only and PPC processes, the coupling of solar radiation with the PPC process shifts the SIE window. As shown in Figure 5a,b, the SIE required to achieve the same toluene conversion and CO_2 selectivity in the SEPPC process is about 52 and 35% lower than that of PPC and NTP-only processes, respectively, suggesting that low energy consumption can be achieved in the SEPPC process. This finding can also be confirmed by the significantly enhanced energy efficiency in Figure 5c. Upon solar illumination, the energy efficiency of the SEPPC process is increased by ∼57% at an SIE of 152 J L^{-1} in comparison to the PPC process, achieving a superior efficiency of 12.7 g kWh^{-1} for toluene conversion, which is among the best in the state-of-the-art studies on plasma oxidation of toluene with and without a catalyst.[18−21]

The enhanced energy efficiency achieved in the SEPPC oxidation of toluene over the MnO_2/GFF catalyst is mainly attributed to the remarkable solar thermal effect on the catalyst. First, the elevated temperature of the catalyst bed because of the heating effect resulted from the solar irradiation promotes the conversion of ozone to active oxygen species including more active O radicals over the MnO_2/GFF catalyst (Figure 6a), which can be confirmed by the decreased ozone

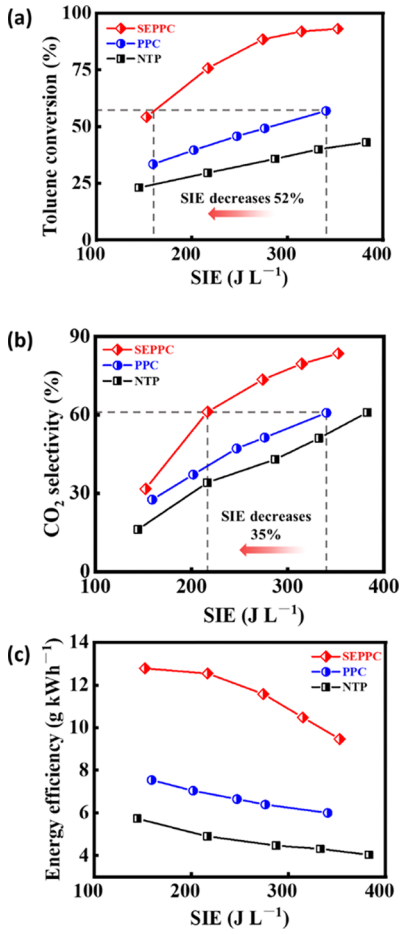

Figure 5. Comparison of the catalytic performance and energy efficiency in the NTP-only, PPC, and SEPPC processes: (a) toluene conversion, (b) CO_2 selectivity, and (c) energy efficiency.

concentration measured at the outlet of the SEPPC process (Figure 6b). Although the catalyst weight (9.8 mg only) used in this work is 10−100 times lower than that used in most of the previous works,[44,62,63] the maximum O_3 decomposition capacity over the MnO_2/GFF catalyst in the PPC process (without solar radiation) reaches up to ∼0.18 g_{O_3} g^{-1} h^{-1}. Moreover, the conversion of ozone (maximum O_3 decomposition capacity) in the SEPPC process is ∼0.52 g_{O_3} g^{-1} h^{-1}, almost triple that of the PPC without the solar radiation counterpart operated at room temperature, which is significantly higher than that in a previous work (∼0.30 g_{O_3} g^{-1} h^{-1}).[20] The active oxygen species formed on the surface of MnO_2/GFF, especially O radicals, have higher oxidative activity compared to ozone,[18] which significantly contributes to the enhanced oxidation of toluene and the reaction intermediates, resulting in higher CO_2 selectivity, higher energy efficiency, and lower CO selectivity (Figure S9a, Supporting Information). Moreover, the carbon balance of the SEPPC process is much higher than that of the PPC process, indicating that the coupling of solar illumination with the PPC process substantially reduced the formation of organic byproducts (Figure S9b, Supporting Information).[64] Note that the concentration of residue ozone after the SEPPC process is significantly lower than that of the PPC process without solar irradiation and the NTP-only process because of

https://dx.doi.org/10.1021/acscatal.9b04844
ACS Catal. 2020, 10, 4420−4432

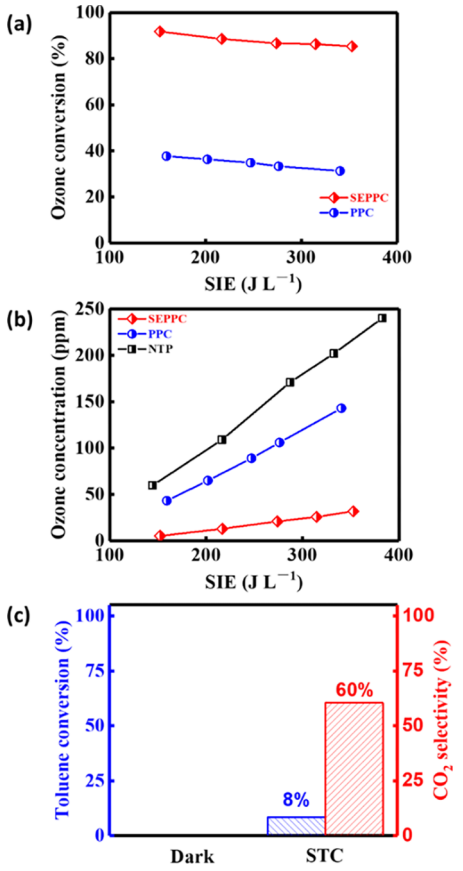

Figure 6. Catalytic performance of the MnO_2/GFF catalyst: (a) catalytic conversion of ozone in PPC and SEPPC processes; (b) ozone concentration in NTP-only, PPC, and SEPPC processes, and (c) catalytic conversion of toluene in the dark and the STC process without NTP.

superior ODC over the MnO_2/GFF catalyst assisted by solar irradiation (Figure 6b).

To get new insights into the contributions of the solar thermal effect and ozone to the SEPPC oxidation of toluene, the catalytic oxidation of toluene in air, with and without solar radiation, was carried out in the absence of ozone. Figure 6c shows that the MnO_2/GFF catalyst has no catalytic activity toward toluene oxidation without solar irradiation (dark). Upon solar irradiation, the elevated temperature of the catalyst bed induced by the solar thermal effect can thermally activate the MnO_2/GFF catalyst, enabling the spontaneous solar thermal catalytic (STC) reaction to proceed. However, the conversion of toluene was only 8% with a CO_2 selectivity of 60%, which can be attributed to the absence of ozone in this reaction and the insufficient activation of lattice oxygen at the relatively low temperature (72.6 °C) induced by the solar irradiation. These results clearly show that the conversion of toluene in the SEPPC is significantly higher than the sum of the toluene conversion using STC and PPC processes, which demonstrates that a clear synergistic effect of the SEPPC process resulted from the coupling of solar irradiation and PPC has been achieved with a SC of ~42% in this work.

The roles of pure MnO_2 and GFF in the SEPPC oxidation of toluene were further investigated. The catalytic performance of pure MnO_2 in the SEPPC and PPC processes is given in Figure S10 (Supporting Information). Compared with MnO_2/GFF, pure MnO_2 exhibits lower toluene conversion, CO_2 selectivity, carbon balance, and energy efficiency in the PPC process. The residual ozone concentration over pure MnO_2 is higher than that of MnO_2/GFF, indicating that the ozone conversion capability of pure MnO_2 is weaker than that of MnO_2/GFF. Under solar irradiation, the catalytic activity of MnO_2 is enhanced because of the heating of the catalyst bed. However, the toluene conversion, CO_2 selectivity, carbon balance, and energy efficiency in the SEPPC process using MnO_2 are still 21, 23, 19, and 15% lower than that of MnO_2/GFF at an SIE of 360 J L^{-1}, respectively, demonstrating that pure MnO_2 (without GFF) is not efficient for the oxidation of toluene in the SEPPC process. As shown in Figure S11 (Supporting Information), the toluene conversion over pure GFF in the SEPPC and PPC processes is ~46.8 and ~46.2%, respectively, at an SIE of 401 J L^{-1}, which is almost the same as that achieved in the NTP-only process (~47.3%). Therefore, pure GFF without MnO_2 loading exhibits no catalytic activity toward toluene oxidation in the SEPPC and PCC processes. These results clearly show that the bifunctional GFF, designed as the catalyst support and light absorber, plays a crucial role in the oxidation of toluene in the SEPPC process. Bifunctional GFF can provide abundant sites for the dispersion of MnO_2 and enhance the absorption of light, elevating the temperature of MnO_2, significantly contributing to the enhanced catalytic activity of the MnO_2/GFF catalyst.

3.3. Catalyst Stability. Catalyst stability is the key to the using plasma-catalytic gas cleaning technology on a commercial scale. Figure 7 shows a comparison of the catalyst stability

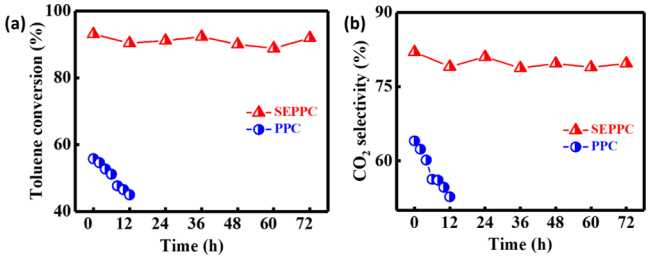

Figure 7. Comparison of the catalytic stability in PPC and SEPPC processes: regarding (a) toluene conversion and (b) CO_2 selectivity.

in the PPC and SEPPC processes. The results clearly show that the MnO_2/GFF catalyst suffers from serious deactivation in the PPC process at room temperature without solar illumination. Specifically, the conversion of toluene decreases from 56 to 45% after the 12 h test at an SIE of 364 J L^{-1}. Similarly, the selectivity of CO_2 in the PPC process decreases significantly after running the reaction for 12 h. In contrast, the MnO_2/GFF catalyst exhibits outstanding stability in the SEPPC process after the 72 h-test at 1 sun (activity loss of <3%), significantly superior to those reported in previous works (e.g., loss of ~16% after 0.5 h[23] and loss of ~50% after 2.5 h[32]). Furthermore, the surface states of the MnO_2/GFF catalyst before and after the 72 h-reaction were analyzed using the C 1s spectra (Figure S12, Supporting Information). The peaks at 284.6, 286.5, 287.6, and 289.1 eV correspond to C═C/C−C, C−O, C═O, and O═C−O bonds, respectively.[65] Although weak oxidation of GFF is detected after the exposure of the catalyst to the ozone flow in the SEPPC and PPC processes for 72 h, the content of the formed C═O and O═C−O bonds is only 3.9 and 3.1%, respectively. In addition, the intensity of C═C/C−C and C−O peaks is almost unchanged, indicating

https://dx.doi.org/10.1021/acscatal.9b04844
ACS Catal. 2020, 10, 4420−4432

that GFF has excellent structural stability. Therefore, we have successfully demonstrated the steady-state toluene conversion at 1 sun via the exploitation of abundant, renewable solar energy, significantly reducing the energy consumption and avoiding the use of external heating devices in the conventional PPC process.

To elucidate the underlying mechanism contributing to the achieved superior stability of the MnO_2/GFF catalyst in the SEPPC oxidation of toluene, a solar-induced regeneration of the deactivated catalyst was carried out using ozone. The characteristics of the fresh, spent, and regenerated catalysts were investigated using FTIR and XPS analysis. Compared with the fresh catalyst, the FTIR spectrum of the spent catalyst exhibits a new absorption peak corresponding to C−O−H bending at 1390 cm^{-1} (Figure 8a), indicating the deposition of

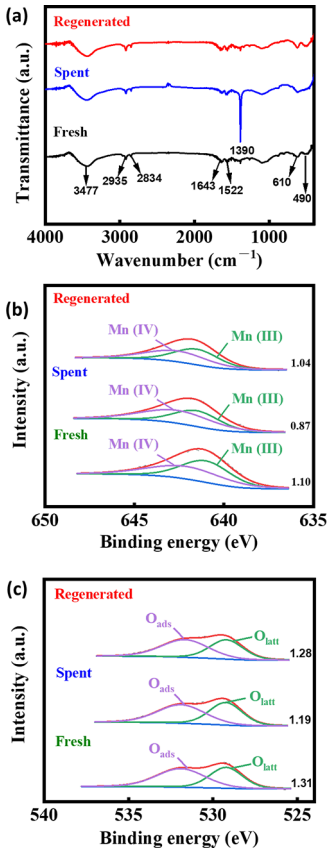

Figure 8. (a) FTIR, (b) Mn 2p, and (c) O 1s spectra of fresh, spent, and regenerated MnO_2/GFF catalysts.

organic intermediates on the catalyst surface.[55] Without solar irradiation, the deposited reaction intermediates on the catalyst cannot be completely removed or oxidized because of the ozone decomposition to more oxidative species on the catalyst being ineffective at room temperature, resulting in the deactivation of the MnO_2/GFF catalyst in the PPC process.[62] Interestingly, this characteristic peak disappears after the solar-induced thermal regeneration of the spent catalyst. The elevated temperature of the catalyst because of solar irradiation promotes the decomposition of ozone, generating more active oxygen species, which significantly contribute to the highly efficient oxidation of intermediates on the catalyst surface.

The change of chemical states on the catalyst surface was examined using XPS, as plotted in Figure 8b,c. The Mn 2p spectra can be split into Mn^{3+} (641.0−641.4 eV) and Mn^{4+} (642.1−642.6 eV) peaks,[49,66,67] whereas the spectra of O 1s fit the O_{latt} (lattice oxygen, 529.2 eV) and O_{ads} (surface adsorbed oxygen, 531.6−531.9 eV) peaks.[59] Higher Mn^{3+}/Mn^{4+} and O_{ads}/O_{latt} ratios represent the presence of more oxygen vacancies, as well as adsorbed oxygen species with a high mobility on the catalyst surface, respectively.[30,31,60,68] Compared to the fresh catalyst, both the Mn^{3+}/Mn^{4+} and O_{ads}/O_{latt} ratios on the spent catalyst after the reaction decrease from 1.10 and 1.31 to 0.87 and 1.19, respectively. In contrast, both ratios on the surface of the solar-induced regenerated catalyst increase and reach 1.04 and 1.28, respectively, demonstrating the self-cleaning capability of the MnO_2/GFF catalyst, regenerating oxygen vacancies and adsorbed oxygen species on the catalyst surface. These promising findings show the unique solar-driven self-cleaning ability of the MnO_2/GFF catalyst in the reaction, which contributes to the superior long-term catalytic stability in the SEPPC oxidation of toluene.

3.4. Reaction Mechanism. Figure 9a shows the formation of byproducts under different process modes. Benzaldehyde,

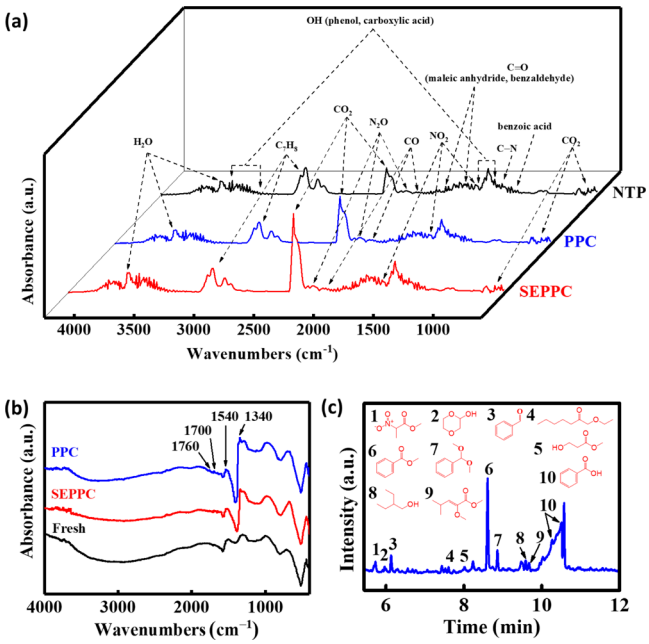

Figure 9. (a) FTIR spectra of toluene oxidation using NTP-only, PPC, and SEPPC. (b) DRIFTS analysis of fresh and spent catalysts (after SEPPC and PPC reactions). (c) GC−MS analysis of a spent catalyst (after the PPC reaction).

benzoic acid, maleic anhydride, and nitrophenol are identified as the byproducts. To be specific, the absorption bands at 3600−3400 and 1600−1450 cm^{-1} correspond to the stretching and bending vibrations of OH groups in organic byproducts (e.g., phenol, carboxylic acid, etc.).[69] The absorption bands at 1900−1800 and 1700−1680 cm^{-1} can be ascribed to the stretching vibrations of C═O groups in maleic anhydride and benzaldehyde, respectively.[70,71] The presence of benzoic acid is confirmed by the bands at 1650−1610, 1550, and 1350−1300 cm^{-1},[72,73] whereas the absorption peaks at 1400−1350 cm^{-1} are related to the C−N stretching vibration.[70] In addition, NO_2 and N_2O are also detected (the absorption bands at 1621 and 2224 cm^{-1}, respectively).[20,58]

Figure 9b shows the DRIFTS analysis of the fresh and spent catalysts (after the SEPPC and PPC reactions). The bands at

https://dx.doi.org/10.1021/acscatal.9b04844
ACS Catal. 2020, 10, 4420−4432

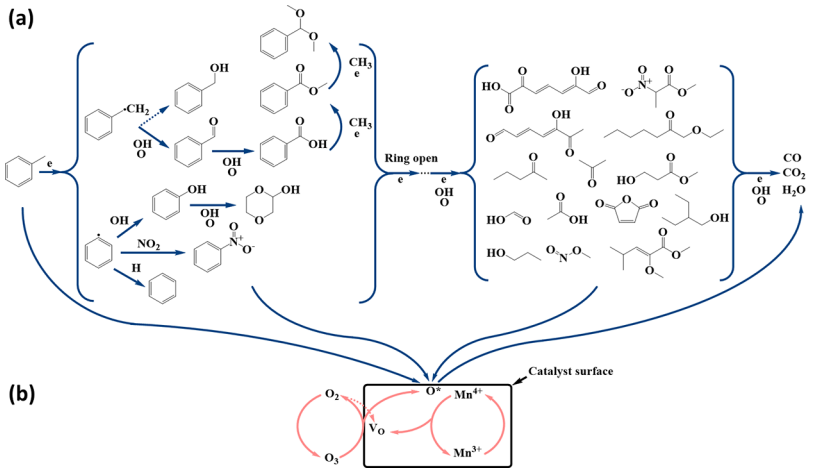

Figure 10. Plausible reaction pathways for toluene conversion in the SEPPC process: (a) NTP induced gas-phase reactions in the plasma zone and (b) solar-enhanced catalytic reactions on the surfaces of MnO_2/GFF.

1340 cm^{-1} correspond to the CH_2 deformation vibration of benzyl species because of the formation of benzyl alcohol.[74] The absorption bands at 1540 cm^{-1} can be assigned to the COO^- stretching vibration of benzoic acid.[75] The characteristic bands at 1700 and 1760 cm^{-1} are ascribed to C═O stretching vibration of benzaldehyde and maleic anhydride, respectively.[75,76] As shown in Figure 9c, different organic intermediates are measured on the surfaces of the spent catalyst using GC−MS (see the Supporting Information & Table S1 for details).

The formation of byproducts under different process modes provides direct evidence to elucidate the plausible dominant reaction pathways in the oxidation of toluene using SEPPC (Figure 10). The oxidation of toluene in the SEPPC process can be attributed to both the gas-phase reaction in the DBD plasma and solar-enhanced catalytic oxidation on MnO_2/GFF.[77] It has been well established that excited nitrogen species (e.g., excited N_2 ($C^3\Pi_u-B^3\Pi_g$)) and oxidative species (e.g., O and OH radicals) generated in air plasmas play critical roles in the stepwise decomposition and oxidation of toluene and its intermediates (Figure 10a).[23,78] Benzyl generated by the H-abstraction of methyl can be oxidized by O or OH to form benzaldehyde, which can be further oxidized to benzoic acid.[79] Benzyl radicals can also be oxidized to produce benzyl alcohol.[80] Benzoic acid could react with methyl radicals and electrons to form benzoic acid, methyl ester, and further generate benzaldehyde dimethyl acetal. In addition, the C−C bond between methyl and the benzene ring can be fractured by excited nitrogen species and electrons to generate methyl and phenyl radicals. Phenyl radicals can react with OH, H, and NO_2 to form phenol, benzene, and nitrobenzene, respectively.[21] Phenol can be further oxidized to 1,4-dioxan-2-ol, as confirmed by the analysis of GC−MS. After that, aromatic intermediates collide with energetic electrons and reactive species, resulting in the rupture of aromatic rings and stepwise oxidation into CO, CO_2, and H_2O.[81]

As shown in Figure 10b, in the solar-induced thermal catalytic reaction, unconverted toluene and reaction intermediates in the plasma gas-phase reaction can be absorbed onto the surface of the MnO_2/GFF catalyst and be further oxidized by active atomic oxygen (O*) species produced over the oxygen vacancies (V_O) from the decomposition of ozone according to the following processes (R1−R3).[30,31,82] The presence of Mn^{3+} in MnO_2/GFF indicates the formation of oxygen vacancies on the catalyst surface because of the electrostatic balance.[83] The transformation of Mn^{4+} to Mn^{3+} in the catalytic reaction can supply oxygen vacancies. In addition, the consumed oxygen vacancies could be replenished by gas-phase oxygen.[23]

$$O_3 + V_O \rightarrow O_2 + O^* \quad \text{(R1)}$$

$$O_3 + O^* \rightarrow O_2 + O_2^* \quad \text{(R2)}$$

$$O_2^* \rightarrow O_2 + V_O \quad \text{(R3)}$$

The conversion of ozone depends on the decomposition rate of the peroxide species (O_2^*).[84] Jia et al. reported that the decomposition of peroxide species could be accelerated by increasing the reaction temperature.[30] Thus, the solar-induced thermal effect enhances the catalytic decomposition of ozone on the surface of MnO_2/GFF, generating more atomic oxygen species, which make a major contribution to the enhanced oxidation of toluene and reaction intermediates. The finding can be confirmed by the significantly higher ozone decomposition (an triple enhancement) in the SEPPC process compared to that of the PPC (without the solar irradiation) counterpart operated at room temperature. Furthermore, the O_3 decomposition capacity over the MnO_2/GFF catalyst with solar irradiation is significantly higher than that reported in previous studies.[20] The concentration of residue ozone after the SEPPC process is considerably lower than that of the PPC process without the solar irradiation and NTP-only process. Note that the catalyst weight (9.8 mg only) used in this work is 10−100 times lower than that used in most of the previous works.[44,62,63] Therefore, the concentration of residue ozone can be further reduced by tuning the weight of the catalyst.

In addition, the Mars-van Krevelen (MVK) mechanism has been generally considered as a major pathway in thermal catalytic oxidation of toluene over MnO_x.[50,85] Lattice oxygen (O_{latt}) on the catalyst surface can oxidize toluene and reaction intermediates but often requires relatively high temperatures to ensure the effective surface mobility of lattice oxygen.[85] In this study, we find that the conversion of toluene was only 8% in the solar thermal catalytic oxidation of toluene on MnO_2 by air (without O_3), which can be ascribed to the weak or insufficient activation of lattice oxygen at the relatively low temperature

https://dx.doi.org/10.1021/acscatal.9b04844
ACS Catal. 2020, 10, 4420−4432

(72.6 °C) induced by the solar irradiation. Thus, the STC oxidation of toluene and reaction intermediates via the MVK mechanism has made a limited contribution to the superior performance achieved in the SEPPC process. Figure 11 shows the plausible reaction mechanisms in the SEPPC oxidation of toluene over the MnO_2/GFF catalyst.

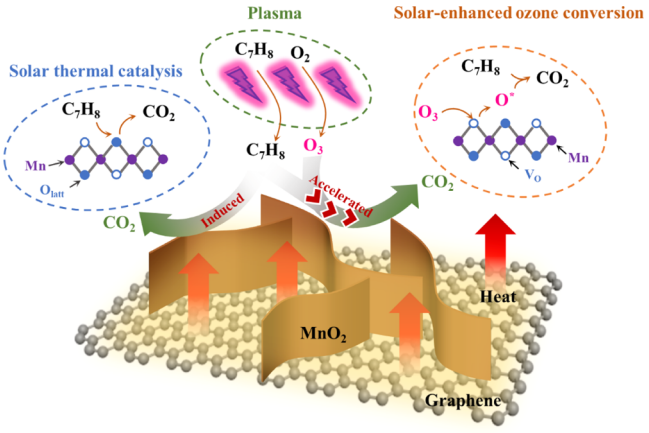

Figure 11. Mechanism of toluene conversion over the hierarchical fin-on-fin MnO_2/GFF catalyst in the SEPPC process.

4. CONCLUSIONS

In this study, we demonstrated that the SEPPC process offers a promising solution for highly efficient oxidation of toluene over the MnO_2/GFF catalyst with a hierarchical fin-on-fin structure. The results show that the bifunctional MnO_2/GFF catalyst with vertical orientation and non-agglomerated morphology can minimize the reflection and transmission of incident light (absorption of >95%), effectively converting the absorbed solar energy into heat, which yields a remarkable temperature rise of 55.6 °C of the catalyst bed under solar irradiation at 1 sun. The amount of MnO_2/GFF catalyst (9.8 mg) was substantially lower (10−100 times lower) than that used in previous works (usually 100−1000 mg). Compared to the PPC process, the coupling of solar illumination with the PPC process significantly enhances the toluene conversion and CO_2 selectivity by 36−63%, reaching up to ∼93 and ∼83%, respectively, at an SIE of ∼350 J L^{-1}, while reducing the energy consumption of the hybrid process by 35−52%. As a result, the SEPPC process exhibits a high energy efficiency of 12.7 g kWh^{-1} for toluene conversion (∼57% higher than that using the PPC process), which is among the highest in the previously reported works. In addition, the MnO_2/GFF catalyst exhibits a superior long-term catalytic stability (activity loss <3%) after running the reaction for 72 h at 1 sun because of its excellent self-cleaning capability induced by solar irradiation. The synergistic effect of solar irradiation and PPC with a SC of ∼42% can be mainly attributed to the solar-induced thermal effect on the catalyst bed, promoting ozone conversion (enhanced by ∼182% compared to PPC) into more oxidative species (e.g., O radicals) and enhancing the catalytic oxidation of toluene and reaction intermediates on the catalyst surface, as well as the self-cleaning capacity of the catalyst at elevated temperatures. By contrast, the thermal catalytic oxidation of toluene and reaction intermediates via the MVK mechanism has a limited contribution to the superior performance achieved in the SEPPC. This work opens a new route to use abundant, renewable solar energy to achieve high-performance and energy-efficient removal of VOCs using the emerging plasma catalytic process. Getting a fundamental understanding of such a promising solar-enhanced plasma-catalytic gas cleaning process using a model VOC compound is the key and the foundation for the further R&D and process optimization toward future industrial applications.

■ ASSOCIATED CONTENT

Supporting Information

The Supporting Information is available free of charge at https://pubs.acs.org/doi/10.1021/acscatal.9b04844.

SEM analysis of MnO_2/GFF, synthesis process of MnO_2/GFF, catalyst characterization (XPS, XRD, TEM, and H_2-TPR), calculation of solar thermal conversion efficiency, catalytic performance (supplement), C 1s spectra of the fresh and spent MnO_2/GFF, and analysis of intermediates on the surface of the spent catalyst (PDF)

■ AUTHOR INFORMATION

Corresponding Authors

Huachao Yang − *State Key Laboratory of Clean Energy Utilization, Institute for Thermal Power Engineering, College of Energy Engineering, Zhejiang University, Hangzhou, Zhejiang Province 310027, China*; Email: huachao@zju.edu.cn

Jianhua Yan − *State Key Laboratory of Clean Energy Utilization, Institute for Thermal Power Engineering, College of Energy Engineering, Zhejiang University, Hangzhou, Zhejiang Province 310027, China*; Email: yanjh@zju.edu.cn

Xin Tu − *Department of Electrical Engineering and Electronics, University of Liverpool, Liverpool L69 3GJ, U.K.*; orcid.org/0000-0002-6376-0897; Email: xin.tu@liverpool.ac.uk

Authors

Zheng Bo − *State Key Laboratory of Clean Energy Utilization, Institute for Thermal Power Engineering, College of Energy Engineering, Zhejiang University, Hangzhou, Zhejiang Province 310027, China*; orcid.org/0000-0001-9308-7624

Shiling Yang − *State Key Laboratory of Clean Energy Utilization, Institute for Thermal Power Engineering, College of Energy Engineering, Zhejiang University, Hangzhou, Zhejiang Province 310027, China*

Jing Kong − *State Key Laboratory of Clean Energy Utilization, Institute for Thermal Power Engineering, College of Energy Engineering, Zhejiang University, Hangzhou, Zhejiang Province 310027, China*

Jinhui Zhu − *State Key Laboratory of Clean Energy Utilization, Institute for Thermal Power Engineering, College of Energy Engineering, Zhejiang University, Hangzhou, Zhejiang Province 310027, China*

Yaolin Wang − *Department of Electrical Engineering and Electronics, University of Liverpool, Liverpool L69 3GJ, U.K.*

Xiaodong Li − *State Key Laboratory of Clean Energy Utilization, Institute for Thermal Power Engineering, College of Energy Engineering, Zhejiang University, Hangzhou, Zhejiang Province 310027, China*; orcid.org/0000-0002-5331-5968

Kefa Cen − *State Key Laboratory of Clean Energy Utilization, Institute for Thermal Power Engineering, College of Energy Engineering, Zhejiang University, Hangzhou, Zhejiang Province 310027, China*

Complete contact information is available at:

https://dx.doi.org/10.1021/acscatal.9b04844
ACS Catal. 2020, 10, 4420−4432

https://pubs.acs.org/10.1021/acscatal.9b04844

Notes

The authors declare no competing financial interest.

■ ACKNOWLEDGMENTS

The authors would like to thank the National Natural Science Foundation of China (no. 51576175) for the financial support. X.T. and Y.W. acknowledge the European Union (EU) and Horizon 2020 funding awarded under the Marie Sklodowska-Curie Action to the EUROPAH Consortium (grant number 722346). The support of Tengfei Liu and Jucan Gao in the Center for Synthetic Biology at Zhejiang University, in carrying out GC−MS analysis, is also appreciatively accredited.

■ REFERENCES

(1) Cohen, A. J.; Brauer, M.; Burnett, R.; Anderson, H. R.; Frostad, J.; Estep, K.; Balakrishnan, K.; Brunekreef, B.; Dandona, L.; Dandona, R.; Freedman, G.; Hubbell, B.; Jobling, A.; Kan, H.; Knibbs, L.; Liu, Y.; Martin, R.; Morawska, L.; Pope, C. A.; Shin, H.; Straif, K.; Shaddick, G.; Thomas, M.; van Dingenen, R.; van Donkelaar, A.; Vos, T.; Murray, C. J. L.; Forouzanfar, M. H. Estimates and 25-year Trends of the Global Burden of Disease Attributable to Ambient Air Pollution: An Analysis of Data from the Global Burden of Diseases Study 2015. *Lancet* **2017**, *389*, 1907−1918.

(2) Odum, J. R.; Jungkamp, T. P. W.; Griffin, R. J.; Forstner, H. J. L.; Flagan, R. C.; Seinfeld, J. H. Aromatics, Reformulated Gasoline, and Atmospheric Organic Aerosol Formation. *Environ. Sci. Technol.* **1997**, *31*, 1890−1897.

(3) Chen, H. L.; Lee, H. M.; Chen, S. H.; Chang, M. B.; Yu, S. J.; Li, S. N. Removal of Volatile Organic Compounds by Single-Stage and Two-Stage Plasma Catalysis Systems: a Review of the Performance Enhancement Mechanisms, Current Status, and Suitable Applications. *Environ. Sci. Technol.* **2009**, *43*, 2216−2227.

(4) Xie, S.; Deng, J.; Liu, Y.; Zhang, Z.; Yang, H.; Jiang, Y.; Arandiyan, H.; Dai, H.; Au, C. T. Excellent Catalytic Performance, Thermal Stability, and Water Resistance of 3DOM Mn_2O_3-Supported Au−Pd Alloy Nanoparticles for the Complete Oxidation of Toluene. *Appl. Catal., A* **2015**, *507*, 82−90.

(5) Wang, Y.; Arandiyan, H.; Liu, Y.; Liang, Y.; Peng, Y.; Bartlett, S.; Dai, H.; Rostamnia, S.; Li, J. Template-Free Scalable Synthesis of Flower-Like $Co_{3-x}Mn_xO_4$ Spinel Catalysts for Toluene Oxidation. *ChemCatChem* **2018**, *10*, 3429−3434.

(6) Liu, Y.; Liu, Y.; Guo, Y.; Xu, J.; Xu, X.; Fang, X.; Liu, J.; Chen, W.; Arandiyan, H.; Wang, X. Tuning SnO_2 Surface Area for Catalytic Toluene Deep Oxidation: On the Inherent Factors Determining the Reactivity. *Ind. Eng. Chem. Res.* **2018**, *57*, 14052−14063.

(7) Van Durme, J.; Dewulf, J.; Leys, C.; Van Langenhove, H. Combining Non-Thermal Plasma with Heterogeneous Catalysis in Waste Gas Treatment: A Review. *Appl. Catal., B* **2008**, *78*, 324−333.

(8) Vandenbroucke, A. M.; Morent, R.; De Geyter, N.; Leys, C. Non-Thermal Plasmas for Non-Catalytic and Catalytic VOC Abatement. *J. Hazard. Mater.* **2011**, *195*, 30−54.

(9) Feng, X.; Liu, H.; He, C.; Shen, Z.; Wang, T. Synergistic Effects and Mechanism of a Non-Thermal Plasma Catalysis System in Volatile Organic Compound Removal: a Review. *Catal. Sci. Technol.* **2017**, *8*, 936−954.

(10) Kim, H.-H.; Teramoto, Y.; Negishi, N.; Ogata, A. A Multidisciplinary Approach to Understand the Interactions of Nonthermal Plasma and Catalyst: A Review. *Catal. Today* **2015**, *256*, 13−22.

(11) Wang, L.; Yi, Y.; Wu, C.; Guo, H.; Tu, X. One-Step Reforming of CO_2 and CH_4 into High-Value Liquid Chemicals and Fuels at Room Temperature by Plasma-Driven Catalysis. *Angew. Chem., Int. Ed.* **2017**, *56*, 13679−13683.

(12) Wang, Y.; Craven, M.; Yu, X.; Ding, J.; Bryant, P.; Huang, J.; Tu, X. Plasma-Enhanced Catalytic Synthesis of Ammonia over a Ni/Al_2O_3 Catalyst at Near-Room Temperature: Insights into the Importance of the Catalyst Surface on the Reaction Mechanism. *ACS Catal.* **2019**, *9*, 10780−10793.

(13) Wang, L.; Yi, Y.; Guo, H.; Tu, X. Atmospheric Pressure and Room Temperature Synthesis of Methanol through Plasma-Catalytic Hydrogenation of CO_2. *ACS Catal.* **2018**, *8*, 90−100.

(14) Zeng, Y. X.; Wang, L.; Wu, C. F.; Wang, J. Q.; Shen, B. X.; Tu, X. Low Temperature Reforming of Biogas over K-, Mg-and Ce-Promoted Ni/Al_2O_3 Catalysts for the Production of Hydrogen Rich Syngas: Understanding the Plasma-Catalytic Synergy. *Appl. Catal., B* **2018**, *224*, 469−478.

(15) Kim, H.-H.; Ogata, A.; Futamura, S. Oxygen Partial Pressure-Dependent Behavior of Various Catalysts for the Total Oxidation of VOCs using Cycled System of Adsorption and Oxygen Plasma. *Appl. Catal., B* **2008**, *79*, 356−367.

(16) Neyts, E. C.; Ostrikov, K.; Sunkara, M. K.; Bogaerts, A. Correction: Plasma Catalysis: Synergistic Effects at the Nanoscale. *Chem. Rev.* **2016**, *116*, 767.

(17) Ye, Z.; Giraudon, J.-M.; De Geyter, N.; Morent, R.; Lamonier, J.-F. The Design of MnO_x Based Catalyst in Post-Plasma Catalysis Configuration for Toluene Abatement. *Catalysts* **2018**, *8*, 91.

(18) Harling, A. M.; Glover, D. J.; Whitehead, J. C.; Zhang, K. The Role of Ozone in the Plasma-Catalytic Destruction of Environmental Pollutants. *Appl. Catal., B* **2009**, *90*, 157−161.

(19) Huang, H.; Ye, D.; Guan, X. The Simultaneous Catalytic Removal of VOCs and O_3 in a Post-Plasma. *Catal. Today* **2008**, *139*, 43−48.

(20) Huang, Y.; Dai, S.; Feng, F.; Zhang, X.; Liu, Z.; Yan, K. A Comparison Study of Toluene Removal by Two-Stage DBD-Catalyst Systems Loading with MnO_x, $CeMnO_x$, and $CoMnO_x$. *Environ. Sci. Pollut. Res. Int.* **2015**, *22*, 19240−19250.

(21) Huang, H.; Ye, D.; Leung, D. Y. C.; Feng, F.; Guan, X. Byproducts and Pathways of Toluene Destruction via Plasma-Catalysis. *J. Mol. Catal. A: Chem.* **2011**, *336*, 87−93.

(22) Dinh, M. T. N.; Giraudon, J.-M.; Lamonier, J.-F.; Vandenbroucke, A.; De Geyter, N.; Leys, C.; Morent, R. Plasma-Catalysis of Low TCE Concentration in Air using $LaMnO_{3+\delta}$ as Catalyst. *Appl. Catal., B* **2014**, *147*, 904−911.

(23) Chang, T.; Shen, Z.; Huang, Y.; Lu, J.; Ren, D.; Sun, J.; Cao, J.; Liu, H. Post-Plasma-Catalytic Removal of Toluene using MnO_2-Co_3O_4 Catalysts and Their Synergistic Mechanism. *Chem. Eng. J.* **2018**, *348*, 15−25.

(24) Huang, L.; Zheng, M.; Yu, D.; Yaseen, M.; Duan, L.; Jiang, W.; Shi, L. In-Situ Fabrication and Catalytic Performance of Co-Mn@CuO Core-Shell Nanowires on Copper Meshes/Foams. *Mater. Des.* **2018**, *147*, 182−190.

(25) Dinh, M. T. N.; Giraudon, J.-M.; Vandenbroucke, A. M.; Morent, R.; De Geyter, N.; Lamonier, J.-F. Post Plasma-Catalysis for Total Oxidation of Trichloroethylene over Ce-Mn Based Oxides Synthesized by a Modified "Redox-Precipitation Route". *Appl. Catal., B* **2015**, *172*−*173*, 65−72.

(26) Nguyen Dinh, M. T.; Giraudon, J.-M.; Vandenbroucke, A. M.; Morent, R.; De Geyter, N.; Lamonier, J.-F. Manganese Oxide Octahedral Molecular Sieve K-OMS-2 as Catalyst in Post Plasma-Catalysis for Trichloroethylene Degradation in Humid Air. *J. Hazard. Mater.* **2016**, *314*, 88−94.

(27) Vandenbroucke, A. M.; Nguyen Dinh, M. T.; Nuns, N.; Giraudon, J.-M.; De Geyter, N.; Leys, C.; Lamonier, J.-F.; Morent, R. Combination of Non-Thermal Plasma and Pd/$LaMnO_3$ for Dilute Trichloroethylene Abatement. *Chem. Eng. J.* **2016**, *283*, 668−675.

(28) Panov, G. I.; Uriarte, A. K.; Rodkin, M. A.; Sobolev, V. I. Generation of Active Oxygen Species on Solid Surfaces. Opportunity for Novel Oxidation Technologies over Zeolites. *Catal. Today* **1998**, *41*, 365−385.

(29) Li, W.; Oyama, S. T. Mechanism of Ozone Decomposition on a Manganese Oxide Catalyst. 2. Steady-state and Transient Kinetic Studies. *J. Am. Chem. Soc.* **1998**, *120*, 9047−9052.

(30) Jia, J.; Zhang, P.; Chen, L. Catalytic Decomposition of Gaseous Ozone over Manganese Dioxides with Different Crystal Structures. *Appl. Catal., B* **2016**, *189*, 210−218.
(31) Rezaei, E.; Soltan, J.; Chen, N. Catalytic Oxidation of Toluene by Ozone over Alumina Supported Manganese Oxides: Effect of Catalyst Loading. *Appl. Catal., B* **2013**, *136*−*137*, 239−247.
(32) Rezaei, E.; Soltan, J. Low Temperature Oxidation of Toluene by Ozone over MnO_x/γ-alumina and MnO_x/MCM-41 Catalysts. *Chem. Eng. J.* **2012**, *198*−*199*, 482−490.
(33) Rezaei, E.; Soltan, J.; Chen, N.; Lin, J. Effect of Noble Metals on Activity of MnO_x/γ-alumina Catalyst in Catalytic Ozonation of Toluene. *Chem. Eng. J.* **2013**, *214*, 219−228.
(34) Licht, S. Efficient Solar-Driven Synthesis, Carbon Capture, and Desalinization, STEP: Solar Thermal Electrochemical Production of Fuels, Metals. *Adv. Mater.* **2011**, *23*, 5592−5612.
(35) Ye, S.; Wang, R.; Wu, M.-Z.; Yuan, Y.-P. A Review on g-C3N4 for Photocatalytic Water Splitting and CO_2 Reduction. *Appl. Surf. Sci.* **2015**, *358*, 15−27.
(36) Lewis, N. S.; Nocera, D. G. Powering the Planet: Chemical Challenges in Solar Energy Utilization. *Proc. Natl. Acad. Sci. U.S.A.* **2006**, *103*, 15729−15735.
(37) Zhang, N.; Yang, M.-Q.; Liu, S.; Sun, Y.; Xu, Y.-J. Waltzing with the Versatile Platform of Graphene to Synthesize Composite Photocatalysts. *Chem. Rev.* **2015**, *115*, 10307−10377.
(38) Zhang, Y.; Chen, Z.; Liu, S.; Xu, Y.-J. Size Effect Induced Activity Enhancement and Anti-Photocorrosion of Reduced Graphene Oxide/ZnO Composites for Degradation of Organic Dyes and Reduction of Cr (VI) in Water. *Appl. Catal., B* **2013**, *140*−*141*, 598−607.
(39) Lu, K.-Q.; Xin, X.; Zhang, N.; Tang, Z.-R.; Xu, Y.-J. Photoredox Catalysis over Graphene Aerogel-Supported Composites. *J. Mater. Chem. A* **2018**, *6*, 4590−4604.
(40) Yi, F.; Ren, H.; Dai, K.; Wang, X.; Han, Y.; Wang, K.; Li, K.; Guan, B.; Wang, J.; Tang, M.; Shan, H.; Zheng, M.; You, Z.; Wei, D.; Liu, Z. Solar Thermal-Driven Capacitance Enhancement of Supercapacitors. *Energy Environ. Sci.* **2018**, *11*, 2016−2024.
(41) Ren, H.; Tang, M.; Guan, B.; Wang, K.; Yang, J.; Wang, F.; Wang, M.; Shan, J.; Chen, Z.; Wei, D.; Peng, Z. Hierarchical Graphene Foam for Efficient Omnidirectional Solar-Thermal Energy Conversion. *Adv. Mater.* **2017**, *29*, 1702590.
(42) Lim, D.-K.; Barhoumi, A.; Wylie, R. G.; Reznor, G.; Langer, R. S.; Kohane, D. S. Enhanced Photothermal Effect of Plasmonic Nanoparticles Coated with Reduced Graphene Oxide. *Nano Lett.* **2013**, *13*, 4075−4079.
(43) Xiong, G.; He, P.; Wang, D.; Zhang, Q.; Chen, T.; Fisher, T. S. Hierarchical Ni−Co Hydroxide Petals on Mechanically Robust Graphene Petal Foam for High-Energy Asymmetric Supercapacitors. *Adv. Funct. Mater.* **2016**, *26*, 5460−5470.
(44) Delagrange, S.; Pinard, L.; Tatibouet, J. Combination of a Non-Thermal Plasma and a Catalyst for Toluene Removal from Air: Manganese Based Oxide Catalysts. *Appl. Catal., B* **2006**, *68*, 92−98.
(45) Falkenstein, Z.; Coogan, J. J. Microdischarge Behaviour in the Silent Discharge of Nitrogen-Oxygen and Water-Air Mixtures. *J. Phys. D: Appl. Phys.* **1997**, *30*, 817.
(46) Yang, S.; Bo, Z.; Yang, H.; Shuai, X.; Qi, H.; Li, X.; Yan, J.; Cen, K. Hierarchical Petal-on-Petal MnO_2/Vertical Graphene Foam for Postplasma Catalytic Decomposition of Toluene with High Efficiency and Ultralow Pressure Drop. *Ind. Eng. Chem. Res.* **2018**, *57*, 15291−15300.
(47) Rakhi, R. B.; Chen, W.; Cha, D.; Alshareef, H. N. Nanostructured Ternary Electrodes for Energy-Storage Applications. *Adv. Energy Mater.* **2012**, *2*, 381−389.
(48) Yang, Y.; Huang, J.; Wang, S.; Deng, S.; Wang, B.; Yu, G. Catalytic Removal of Gaseous Unintentional POPs on Manganese Oxide Octahedral Molecular Sieves. *Appl. Catal., B* **2013**, *142*−*143*, 568−578.
(49) Lu, L.; Tian, H.; He, J.; Yang, Q. Graphene−MnO_2 Hybrid Nanostructure as a New Catalyst for Formaldehyde Oxidation. *J. Phys. Chem. C* **2016**, *120*, 23660−23668.
(50) Wang, J.; Zhang, G.; Zhang, P. Graphene-Assisted Photothermal Effect on Promoting Catalytic Activity of Layered MnO_2 for Gaseous Formaldehyde Oxidation. *Appl. Catal., B* **2018**, *239*, 77−85.
(51) Li, Z. Q.; Lu, C. J.; Xia, Z. P.; Zhou, Y.; Luo, Z. X-ray Diffraction Patterns of Graphite And Turbostratic Carbon. *Carbon* **2007**, *45*, 1686−1695.
(52) Fan, Z.; Yan, J.; Wei, T.; Zhi, L.; Ning, G.; Li, T.; Wei, F. Asymmetric Supercapacitors Based on Graphene/MnO_2 and Activated Carbon Nanofiber Electrrodes with High Power and Energy Density. *Adv. Funct. Mater.* **2011**, *21*, 2366−2375.
(53) Li, G.; Lu, Y.; Cheng, L.; Zhu, M.; Zhai, C.; Du, Y.; Ping, Y. Efficient Catalytic Ozonation of Bisphenol-A over Reduced Graphene Oxide Modified Sea Urchin-Like A-MnO_2 Architectures. *J. Hazard. Mater.* **2015**, *294*, 201−208.
(54) Liu, X.; Shi, L.; Jiang, W.; Zhang, J.; Huang, L. Taking Full Advantage of $KMnO_4$ in Simplified Hummers Method: A green and One Pot Process for the Fabrication of Alpha MnO_2 Nanorods on Graphene Oxide. *Chem. Eng. Sci.* **2018**, *192*, 414−421.
(55) Hu, M.; Hui, K. S.; Hui, K. N. Role of Graphene in MnO_2/Graphene Composite for Catalytic Ozonation of Gaseous Toluene. *Chem. Eng. J.* **2014**, *254*, 237−244.
(56) He, Y.; Chen, W.; Li, X.; Zhang, Z.; Fu, J.; Zhao, C.; Xie, E. Freestanding Three-Dimensional Graphene/MnO_2 Composite Networks as Ultralight and Flexible Supercapacitor Electrodes. *ACS Nano* **2013**, *7*, 174.
(57) Julien, C.; Massot, M.; Baddour-Hadjean, R.; Franger, S.; Bach, S.; Pereira-Ramos, J. Raman Spectra of Birnessite Manganese Dioxides. *Solid State Ionics* **2003**, *159*, 345−356.
(58) Li, Y.; Fan, Z.; Shi, J.; Liu, Z.; Shangguan, W. Post Plasma-Catalysis for VOCs Degradation over Different Phase Structure MnO_2 Catalysts. *Chem. Eng. J.* **2014**, *241*, 251−258.
(59) Sang, C. K.; Wang, G. S. Catalytic Combustion of VOCs over a Series of Manganese Oxide Catalysts. *Appl. Catal., B* **2010**, *98*, 180−185.
(60) Li, Y.; Fan, Z.; Shi, J.; Liu, Z.; Zhou, J.; Shangguan, W. Modified Manganese Oxide Octahedral Molecular Sieves M′-OMS-2 (M′=Co,Ce,Cu) as Catalysts in Post Plasma-Catalysis for Acetaldehyde Degradation. *Catal. Today* **2015**, *256*, 178−185.
(61) Lin, X.; Li, S.; He, H.; Wu, Z.; Wu, J.; Chen, L.; Ye, D.; Fu, M. Evolution of Oxygen Vacancies in MnO_x-CeO_2 Mixed Oxides for Soot Oxidation. *Appl. Catal., B* **2018**, *223*, 91−102.
(62) Tang, X.; Feng, F.; Ye, L.; Zhang, X.; Huang, Y.; Liu, Z.; Yan, K. Removal of Dilute VOCs in Air by Post-Plasma Catalysis over Ag-Based Composite Oxide Catalysts. *Catal. Today* **2013**, *211*, 39−43.
(63) Ye, L.; Feng, F.; Liu, J.; Tang, X.; Zhang, X.; Huang, Y.; Liu, Z.; Yan, K. Toluene Decomposition by a Two-stage Hybrid Plasma Catalyst System in Dry Air. *IEEE Trans. Plasma Sci.* **2014**, *42*, 3529−3538.
(64) Veerapandian, S.; Leys, C.; De Geyter, N.; Morent, R. Abatement of VOCs Using Packed Bed Non-Thermal Plasma Reactors: A Review. *Catalysts* **2017**, *7*, 113.
(65) Huh, S.; Park, J.; Kim, Y. S.; Kim, K. S.; Hong, B. H.; Nam, J.-M. UV/Ozone-Oxidized Large-Scale Graphene Platform with Large Chemical Enhancement in Surface-Enhanced Raman Scattering. *ACS Nano* **2011**, *5*, 9799−9806.
(66) Subrahmanyam, C.; Renken, A.; Kiwi-Minsker, L. Catalytic Non-Thermal Plasma Reactor for Abatement of Toluene. *Chem. Eng. J.* **2010**, *160*, 677−682.
(67) Arandiyan, H.; Dai, H.; Deng, J.; Wang, Y.; Xie, S.; Li, J. Dual-Templating Synthesis of Three-Dimensionally Ordered Macroporous $La_{0.6}Sr_{0.4}MnO_3$-Supported Ag Nanoparticles: Controllable Alignments and Super Performance for the Catalytic Combustion of Methane. *Chem. Commun.* **2013**, *49*, 10748−10750.
(68) Gopi, T.; Swetha, G.; Chandra Shekar, S.; Ramakrishna, C.; Saini, B.; Krishna, R.; Rao, P. V. L. Catalytic Decomposition of Ozone on Nanostructured Potassium and Proton Containing δ-MnO_2 Catalysts. *Catal. Commun.* **2017**, *92*, 51−55.
(69) Rodrigues, A.; Tatibouët, J.-M.; Fourré, E. Operando DRIFT Spectroscopy Characterization of Intermediate Species on Catalysts

https://dx.doi.org/10.1021/acscatal.9b04844
ACS Catal. 2020, 10, 4420−4432

Surface in VOC Removal from Air by Non-Thermal Plasma Assisted Catalysis. *Plasma Chem. Plasma Process.* **2016**, *36*, 901−915.
(70) Xu, X.; Wang, P.; Xu, W.; Wu, J.; Chen, L.; Fu, M.; Ye, D. Plasma-Catalysis of Metal Loaded SBA-15 for Toluene Removal: Comparison of Continuously Introduced and Adsorption-Discharge Plasma System. *Chem. Eng. J.* **2016**, *283*, 276−284.
(71) Ma, T.; Qiong, Z.; Jianqi, L.; Fangchuan, Z. Study of Humidity Effect on Benzene Decomposition by the Dielectric Barrier Discharge Nonthermal Plasma Reactor. *Plasma Sci. Technol.* **2016**, *18*, 686.
(72) Hernández-Alonso, M. D.; Tejedor-Tejedor, I.; Coronado, J. M.; Anderson, M. A. Operando FTIR Study of the Photocatalytic Oxidation of Methylcyclohexane and Toluene in Air over TiO_2−ZrO_2 Thin Films: Influence of the Aromaticity of the Target Molecule on Deactivation. *Appl. Catal., B* **2011**, *101*, 283−293.
(73) Xu, W.; Wang, N.; Chen, Y.; Chen, J.; Xu, X.; Yu, L.; Chen, L.; Wu, J.; Fu, M.; Zhu, A. In situ FT-IR study and evaluation of toluene abatement in different plasma catalytic systems over metal oxides loaded γ-Al_2O_3. *Catal. Commun.* **2016**, *84*, 61−66.
(74) Méndez-Román, R.; Cardona-Martínez, N. Relationship between the Formation of Surface Species and Catalyst Deactivation during the Gas-Phase Photocatalytic Oxidation of Toluene. *Catal. Today* **1998**, *40*, 353−365.
(75) Besselmann, S.; Löffler, E.; Muhler, M. On the Role of Monomeric Vanadyl Species in Toluene Adsorption And Oxidation on V_2O_5/TiO_2 Catalysts: A Raman and in situ DRIFTS Study. *J. Mol. Catal. A: Chem.* **2000**, *162*, 401−411.
(76) Centi, G.; Perathoner, S.; Tonini, S. In situ DRIFT Study of the Reactivity and Reaction Mechanism of Catalysts Based on Iron−Molybdenum Oxides Encapsulated in Boralite for the Selective Oxidation of Alkylaromatics. *Catal. Today* **2000**, *61*, 211−221.
(77) Zhu, X.; Liu, S.; Cai, Y.; Gao, X.; Zhou, J.; Zheng, C.; Tu, X. Post-Plasma Catalytic Removal of Methanol over Mn-Ce Catalysts in an Atmospheric Dielectric Barrier Discharge. *Appl. Catal., B* **2016**, *183*, 124−132.
(78) Zhu, X.; Gao, X.; Qin, R.; Zeng, Y.; Qu, R.; Zheng, C.; Tu, X. Plasma-Catalytic Removal of Formaldehyde over Cu−Ce Catalysts in a Dielectric Barrier Discharge Reactor. *Appl. Catal., B* **2015**, *170−171*, 293−300.
(79) Ogata, A.; Ito, D.; Mizuno, K.; Kushiyama, S.; Gal, A.; Yamamoto, T. Effect of Coexisting Components on Aromatic Decomposition in a packed-Bed Plasma Reactor. *Appl. Catal., A* **2002**, *236*, 9−15.
(80) Jiang, N.; Zhao, Y.; Qiu, C.; Shang, K.; Lu, N.; Li, J.; Wu, Y.; Zhang, Y. Enhanced Catalytic Performance of CoO_x-CeO_2 for Synergetic Degradation of Toluene in Multistage Sliding Plasma System through Response Surface Methodology (RSM). *Appl. Catal., B* **2019**, *259*, 118061.
(81) Yi, H.; Yang, X.; Tang, X.; Zhao, S.; Xie, X.; Feng, T.; Ma, Y.; Cui, X. Performance and Pathways of Toluene Degradation over Co/13X by Different Processes Based on Nonthermal Plasma. *Energy Fuels* **2017**, *31*, 11217−11224.
(82) Li, J.; Na, H.; Zeng, X.; Zhu, T.; Liu, Z. In situ DRIFTS Investigation for the Oxidation of Toluene by Ozone over Mn/HZSM-5, Ag/HZSM-5 and Mn−Ag/HZSM-5 Catalysts. *Appl. Surf. Sci.* **2014**, *311*, 690−696.
(83) Wang, F.; Dai, H.; Deng, J.; Bai, G.; Ji, K.; Liu, Y. Manganese Oxides with Rod-, Wire-, Tube-, and Flower-Like Morphologies: Highly Effective Catalysts for the Removal of Toluene. *Environ. Sci. Technol.* **2012**, *46*, 4034−4041.
(84) Radhakrishnan, R.; Oyama, S. T.; Chen, J. G.; Asakura, K. Electron Transfer Effects in Ozone Decomposition on Supported Manganese Oxide. *J. Phys. Chem. B* **2001**, *105*, 4245−4253.
(85) Todorova, S.; Naydenov, A.; Kolev, H.; Holgado, J. P.; Ivanov, G.; Kadinov, G.; Caballero, A. Mechanism of Complete N-Hexane Oxidation on Silica Supported Cobalt and Manganese Catalysts. *Appl. Catal., A* **2012**, *413−414*, 43−51.

https://dx.doi.org/10.1021/acscatal.9b04844
ACS Catal. 2020, 10, 4420−4432